Journal of Materials Chemistry A

Enhanced Thermoelectric Performance of Bi-Sb-Te/Sb2O3 Nanocomposites by Energy Filtering Effect

Journal:	*Journal of Materials Chemistry A*
Manuscript ID	TA-ART-08-2018-008238.R1
Article Type:	Paper
Date Submitted by the Author:	10-Oct-2018
Complete List of Authors:	Pakdel, Amir; National Institute for Materials Science, International Center for Materials Nanoarchitectonics (MANA); University of Dublin Trinity College, Department of Chemistry, CRANN & AMBER Centres Guo, Quansheng; National Institute for Materials Science, Thermal Energy Materials Group Nicolosi, Valeria; Trinity College Dublin, School of Chemistry, School of Physics & CRANN Mori, Takao; National Institute for Materials Science,

Journal Name

ARTICLE

Enhanced Thermoelectric Performance of Bi-Sb-Te/Sb_2O_3 Nanocomposites by Energy Filtering Effect

Received 00th January 20xx,
Accepted 00th January 20xx

DOI: 10.1039/x0xx00000x

www.rsc.org/

Amir Pakdel,*[a,b] Quansheng Guo,[a] Valeria Nicolosi,[b] and Takao Mori *[,a]

Engineering of thermoelectric materials through hybridization with nanoparticles has been proved effective to boost their thermoelectric efficiency by providing the means to decouple thermal and electrical transport phenomena. Here, we report the synthesis of p-type $Bi_{0.5}Sb_{1.5}Te_3$/X wt.% Sb_2O_3 (X=0, 1, 2, 4, 6) nanocomposites, in which the Sb_2O_3 nanoparticles are dispersed mainly at the grain boundaries of the $Bi_{0.5}Sb_{1.5}Te_3$ matrix. It is shown that incorporation of up to 4 wt.% Sb_2O_3 into the matrix results in simultaneous enhancement of the Seebeck coefficient (by filtering of low energy charge carriers) and decline of thermal conductivity (mainly by charge carrier scattering at the interfaces), both of which contribute to improving the thermoelectric figure of merit to a maximum of 1.51 at 350 K. Moreover, the nanocomposites with 2, 4, and 6 wt.% Sb_2O_3 demonstrate ZT>1.0 up to 450 K, making them commercially appealing for thermoelectric applications at a wide temperature range. Furthermore, it is shown that $Bi_{0.5}Sb_{1.5}Te_3$/4 wt.% Sb_2O_3 samples exhibit excellent thermal and chemical stability in ambient atmpsphere and 300–475 K temperature range over a 24-month period.

1. Introduction

Access to energy is a key element for human wellbeing and economic growth; however, providing sufficient energy to satisfy the mounting demand is an ongoing challenge for global development. Unfortunately, our primary energy systems have detrimental environmental impacts as they are dominated by fossil fuels which produce carbon dioxide (CO_2) and other greenhouse gases- the major cause of global climate change. Thus, the world needs a significant transition in its energy sources toward sustainable and renewable power production. One attractive approach in this regard is the harvesting of energy from waste heat by using thermoelectric materials and devices.[1, 2] The ability of a material to convert heat into electricity is evaluated by the dimensionless figure of merit $ZT = \sigma S^2 T/K$, where σ is the electrical conductivity, S is the Seebeck coefficient, and K is the thermal conductivity. These parameters are interrelated and are basically determined by transportation of charge carriers and phonons. Thus, decoupling of the electrical and thermal transport properties by nanostructuring and/or addition of nanosized 2nd phases to thermoelectric materials has become the research focus in this field. With this approach, thermal conductivity is reduced by the scattering of long-wavelength phonons at the interfaces. However, the electrical conductivity will not be affected significantly due to the difference in the mean-free-path of phonons and electrons.[3-7]

Another benefit that may arise from the application of nano-sized 2nd phases in thermoelectric materials is the improvement of the Seebeck coefficient by energy filtering.[8-12] In this case, only charge carriers with high enough energies can overpass the interfacial potential barriers. Nishio and Hirano[13] suggested that the charge carriers with energies lower than the chemical potential have an opposite contribution to thermopower as compared to charge carriers with higher energies. Therefore, the elimination of lower energy charge carriers at potential barriers can increase the absolute value of the thermopower.

Bi-Sb-Te and Bi-Se-Te based alloys exhibit an excellent combination of thermal and electrical properties for thermoelectric energy conversion in the temperature range of 300–500 K.[14] Therefore, there has been a great interest in their application in near-room temperature thermoelectric devices. Following the nanostructuring approach, the figure of merit of these materials reach ~1.0,[15] a suitable threshold value for commercial use. Recent works on their hybridisation with nanoparticles demonstrate even additional ZT enhancements, as well as better mechanical properties. Improvement of the Seebeck coefficient in nanocomposites of $Bi_{0.4}Sb_{1.6}Te_3/SiO_2$,[16] $Bi_{0.5}Sb_{1.5}Te_3/Y_2O_3$,[17] $Bi_{0.4}Sb_{1.6}Te_3/Zn_4Sb_3$,[18] $Bi_2Se_{0.3}Te_{2.7}/Al_2O_3$,[19] $Bi_{0.3}Sb_{1.7}Te_3$/SiC,[20] $Bi_2Te_{2.7}Se_{0.3}$/InSb,[21] and

[a] International Center for Materials Nanoarchitechtonics (WPI-MANA), National Institute for Materials Science (NIMS), Namiki 1-1, Tsukuba 305-0044, Japan.
[b] Centre for Research on Adaptive Nanostructures and Nanodevices (CRANN), Advanced Materials Bio-Engineering Research Centre (AMBER), School of Chemistry, Trinity College Dublin, Pearse Street, Dublin 2, Ireland.
*Email: pakdela@tcd.ie, mori.takao@nims.go.jp

Electronic Supplementary Information (ESI) available: Variation of Seebeck coefficient, electrical conductivity, and thermal conductivity with temperature in all tested samples. See DOI: 10.1039/x0xx00000x

This journal is © The Royal Society of Chemistry 20xx

Please do not adjust margins

$Bi_{0.5}Sb_{1.5}Te_3/ZnO$,[22] are some of the successful examples of energy filtering effect in Bi-Sb-Te and Bi-Se-Te based systems, whilst there are other reports in which the Seebeck coefficient declined after addition of the 2nd phase nanostructures to the matrix; such as, $Bi_2Te_{2.2}Se_{0.8}/SiC$,[23, 24] $Bi_{0.4}Sb_{1.6}Te_3/CuAlO_2$,[25] $Bi_2Te_{2.7}Se_{0.3}/SnS_2$,[26] $Bi_{1.8}Sb_{0.2}Te_{2.85}Se_{0.15}/SbI_3$,[27] and $Bi_{0.48}Sb_{1.52}Te_3/MnSb_2Se_4$.[28]

Inspired by the energy-filtering-effect approach to improve the thermoelectric properties, we explored the influence of Sb_2O_3 nanoparticles addition on the thermoelectric behaviour of $Bi_{0.5}Sb_{1.5}Te_3$ matrix consisting of mixed micro- and nano-sized grains. In these composites, the Sb_2O_3 nanoparticles were abundantly distributed in the $Bi_{0.5}Sb_{1.5}Te_3$ grain boundaries, thus promoting the charge carrier scattering phenomena. This approach was successful in improving the Seebeck coefficient of the nanocomposites and reducing the electronic component of thermal conductivity. The electrical conductivity decreased as well, but the overall power factor and ZT values were enhanced up to 39% at room temperature and 53% at 450 K. Moreover, to evaluate the thermal and chemical stability of the produced nanocomposites and test their high-ZT reproducibility time-dependent property measurements were performed over a 24-month time span.

2. Experimental

2.1. Synthesis and thermomechanical processing of Bi-Sb-Te alloys and composites

Samples with a nominal composition of $Bi_{0.5}Sb_{1.5}Te_3$ (from now on referred to as BST) were prepared from stochiometric quantities of Bi (−100 mesh, ≥99.99%, Sigma Aldrich), Sb (-100 mesh, 99.5%, Sigma Aldrich), and Te (−200 mesh, >99.8%, Sigma Aldrich) powders. The powders were mixed and sealed in an evacuated quartz tube without any intentional dopants. The mixture inside the ampule was melted in an electric furnace at 970 K and slowly cooled to room temperature during 48 h. Then room temperature mechanical processing was performed as following: (i) mechanical milling for 30 min, 2 h, or 4 h; (ii) mechanical milling for 4 h followed by ball milling for 4 h. The resulting powders, with a wide range of nm to μm sizes, were mixed, loaded into a graphite die (Φ 10 mm), and sintered by spark plasma sintering (SPS-1080 System, SPS SYNTEX Inc.) under a uniaxial pressure of 46 MPa. The sintering was performed in an inert argon atmosphere at 808 K for 5 min.

To manufacture composite samples, Sb_2O_3 nanoparticles (<200 nm, >99.9%, Sigma Aldrich) were mixed with milled $Bi_{0.5}Sb_{1.5}Te_3$ particles at 1.0, 2.0, 4.0, and 6.0 wt.% ratios. They were then consolidated by SPS at 808 K for 5 min under a uniaxial pressure of 46 MPa.

2.2. Chemical and structural characterization

The phase compositions were characterized by powder X-ray diffraction (Rigaku, Ultima III) with Cu Kα radiation. Microstructural and chemical composition analysis of the samples was performed by a field-emission ultra high resolution scanning electron microscope (SEM; SU8200 Hitachi) equipped with an energy-dispersive spectrometer (EDS) and an energy-filtered back-scattered electron detector. Structural and localized chemical composition analyses of the samples were performed by a high-resolution field emission transmission electron microscope (JEOL, JEM-2100F) equipped with EDS and an annular scanning transmission electron microscope (STEM) detector.

2.3. Physical property measurements

The thermal diffusivity coefficient (D) was measured using a laser flash thermal analyser (ULVAC TC-7000). The heat capacity (C_p) was measured using a differential scanning calorimetry method (DSC, Netzsch STA 449). The total thermal conductivity (k) was then calculated using the formula $k = D.\rho.C_p$, in which ρ is the density of the sample, obtained from its mass to volume ratio. To calculate the electronic thermal conductivity, the Wiedemann–Franz law ($k_e = \sigma.L.T$) was used. The Lorenz number (L) was calculated as a function of temperature using the Fermi integral function. The electronic thermal conductivity was subtracted from the total thermal conductivity to obtain lattice thermal conductivity (k_l). The sintered disks were cut into rectangular bars for simultaneous electrical conductivity and Seebeck coefficient measurements using a commercial instrument (ZEM-2, ULVAC Shinku-Riko, Japan) with a standard four-probe configuration under a helium atmosphere. To ensure the physical property measurements accuracy, in each case 3 samples were tested, and the intermediate values were reported in the figures. To avoid cluttering in the figures, the recorded values of Seebeck coefficient, electrical conductivity, and thermal conductivity of other samples are provided in the electronic supplementary information. The Hall effect measurement was carried out on the intermediate samples using the Quantum Design physical properties measurement system (PPMS) with the AC transport option, with the magnetic field sweeping from −5 to +5 T. That is, in each case the reported electrical and carrier transport properties come from the same sample.

3. Results and discussion

3.1. Microstructure and chemical composition

Figure 1(a) shows an SEM image of micro- and nano-sized powders of BST mixed with Sb_2O_3 nanoparticles before sintering, and their corresponding EDS analysis. Peaks of Bi, Sb, Te, and O can be identified from the powder mixture, and the other peaks (Al, C, and Be) are associated with the SEM sample holder and substrate. Figure 1(b) exibits the XRD patterns of pure BST alloy and BST/4 wt.% Sb_2O_3 nanocomposite samples after SPS. All peaks are indexed to Bi-Sb-Te phase (COD#1530822, PDF#721836, and JCPDS#49-1713), with a R-3m rhombohedral structure. A small peak of Sb_2O_3 phase (121), with a P-$2_12_12_1$ orthorhombic structure, was identified in the shoulder of the BST (105) peak in the 6 wt.% sample, as shown with an arrow. No obvious impurity phase was found other than the two constituent phases (i.e. BST and Sb_2O_3). A clearer indication of the Sb_2O_3 phase is presented in Figure 1(c), where the XRD patterns of pure BST and BST/6 wt.% Sb_2O_3 are superimposed and magnified. Figure 1(d) shows an

This journal is © The Royal Society of Chemistry 20xx

Please do not adjust margins

SEM image of a sintered nanocomposite sample together with its corresponding EDS line scan analysis. The chemical element content of O and Sb increase at the interface between the particles and the matrix, but the opposite trend is noticed for Te and Bi. This confirms the composition of the nanoparticles as antimony oxide and demonstrates that the nanoparticles were chemically stable in the matrix phase during the SPS process.

Figure 2 depicts SEM images of fracture surfaces of pure BST and its nanocomposite samples consolidated by SPS. Figures 2(a)-(d) show low magnification fractographs of BST samples with 0, 1, 4, and 6 wt.% Sb_2O_3. Figures 2(e)-(f) represent higher magnification images of the fracture surfaces. It is noticed that the addition of Sb_2O_3 nanoparticles reduced average size of the BST grains due to Zenner pinning effect, in which the dispersed 2nd phase particles in a matrix can act as pinning sites, supressing grain growth during the hot compaction process.[29] The presence of Sb_2O_3 nanoparticles at the grain boundaries of the BST matrix (Figure 2(f)) supports this argument. This phenomenon can increase the matrix material's hardness and enhance scattering mechanisms in favour of thermal conductivity diminution. However, Figures 2(d) and (f) suggest that higher levels of particle agglomeration took place in 6 wt.% samples, as a result of which grain refinement and scattering phenomena become less effective.

A representative high resolution TEM image of a pure BST sample in Figure 3(a) shows the synthesized sample's high crystallinity. The higher magnification HR-TEM image in Figure 3(b) demonstrates atomic arrays of Bi and Sb/Te in the structure and the corresponding electron diffraction pattern in Figure 3(c) confirms the high level of purity and crystallinity in the BST sample. The HR-TEM image in Figure 3(b) corelates well with the atomic structure of layered BST in Figure 3(d) in which quintuple layers of Te-Bi-Te-Bi-Te are stacked on top of each other with van der Waals bonding between neighbouring Te atoms. Figure 3(e), a representative dark-field STEM image of a nanocomposite sample, shows the size distribution of nanoparticles in the BST matrix, and its EDS line-scan analysis confirms the chemical composition of the particles as Sb_2O_3.

3.2. Thermoelectric properties

Figure 4(a) shows the temperature dependence of the Seebeck coefficient for p-type BST/X wt.% Sb_2O_3 (X= 0, 1, 2, 4, and 6) samples between 300 and 475 K. The positive values of the Seebeck coefficient in all samples over the entire measuring temperature range indicate that the major charge carriers in pure BST and its composites with Sb_2O_3 nanoparticles were holes (i.e. p-type semiconducting behaviour). It is noticed that the Seebeck coefficient of all samples initially increased with temperature, and after reaching a maximum value decreased. This is due to the excitation of minority carriers (i.e. electrons) at elevated temperatures. As pure BST has a small band gap of only ~0.2 eV, there are a significant number of minority carriers present at high temperatures whose thermoelectric effect opposes that of the majority carriers.[30] In fact, the measured Seebeck coefficient arising from the bipolar effect is a weighted average of two Seebeck coefficients contributed by electrons in the conduction band and holes in the valance band, expressed as:

$$S = \frac{S_n\sigma_n + S_p\sigma_p}{\sigma_n + \sigma_p} \quad (1)$$

where S is the Seebeck coefficient, σ is the electrical conductivity, and n and p represent electron- and hole-related transport processes. Since the Seebeck coefficients for the two carriers are of opposite signs, the magnitude of S reduces upon bipolar thermodiffusion at elevated temperatures.

The Seebeck coefficient of pure BST at room temperature was ~184 μV/K, but after the dispersion of 1, 2 and 4 wt.% Sb_2O_3 nanoparticles, the S value increased to 188, 196, and 205 μV/K respectively, that is a maximum of ~11% enhancement at room temperature. The Seebeck coefficient improvement by adding Sb_2O_3 was more pronounced at higher temperatures, and reached a ~24% enhancement at 475 K. However, when the Sb_2O_3 content increased from 4 to 6 wt.%, the Seebeck coefficient slightly decreased. Another interesting feature noticed in the nanocomposite samples was the gradual shift of the maximum S from 325 K in pure BST to 375 K in 1 wt.% samples, and 400 K in 2, 4, and 6 wt.% samples. Moreover, the S values in nanocomposites were very close between 325 and 450 K, and the values did not drop abruptly by temperature, contrary to the case of pure BST. This indicates that the nanocomposites have a stable and high thermoelectric efficiency in a wider range of temperature, as compared to the pure BST.

Better description of these results requires a comprehensive understanding of the band structure in the samples. Changes in the electronic structure are reflected in the carrier's effective mass, which in turn influences Seebeck coefficient of the specimens. This can be evaluated by the following equations from Boltzmann transport theory,[31] and using the single parabolic band (SPB) model approximation,[32, 33] assuming that the dominant mechanism of charge carrier scattering in pure BST samples is by acoustic phonons:

The Seebeck coefficient,

$$S(\eta) = \frac{k_B}{q}\left[\frac{(r+5/2)F_{(r+3/2)}(\eta)}{(r+3/2)F_{(r+1/2)}(\eta)} - \eta\right] \quad (2)$$

and the Fermi integral,

$$F_i(\eta) = \int_0^\infty \frac{x^i dx}{1+\exp(x-\eta)} \quad (3)$$

the Hall carrier concentration,

$$p_H = 4\pi\left(\frac{2m^*k_BT}{h^2}\right)^{3/2} F_{(1/2)}(\eta) \quad (4)$$

or

$$p_H = \frac{(2m^*k_BT)^{3/2}}{2\pi^2\hbar^3} F_{(1/2)}(\eta) \quad (5)$$

in which, η is the reduced Fermi level, k_B is the Boltzmann constant, q is the elementary charge, r is the scattering

parameter, R_H is the Hall coefficient, m^* is the density of state effective mass, T is the absolute temperature, h is the Planck constant, and ħ is the reduced Planck constant. When charge carriers are scattered by acoustic phonons, we can assume r = – ½ in Equation (2). [31] At 300 K, these equations suggest a density of state effective mass of m* = 1.25m_0 for pure BST, where m_0 is the free charge carrier mass. Alternatively, if we assume a non-parabolic band structure, in which r = ½, the m* relation with carrier concentration can be defined as :[34]

$$p_H = 5.437 \times 10^{15} \left(\frac{m^*}{m_0} T\right)^{3/2} \int_0^{\infty} \frac{x^{1/2}(1+\beta x)^{1/2}(1+2\beta x)}{1+\exp(x-\eta)} dx \quad (6)$$

where β is a non-parabolic coefficient (assumed to be 0.1). This gives a density of state effective mass of m* = 0.68m_0.

These m* values were used to plot Pisarenko lines in Figure 4(b) that demonstrate carrier concentration dependence of the Seebeck coefficient in degenerate semiconductors via the following equation:

$$S = \frac{8\pi^2 k_B^2 T}{3eh^2} m^* \left(\frac{\pi}{3p_H}\right)^{2/3} \quad (7)$$

This plot clarifies the electronic transport behaviour difference in pure BST and BST/Sb_2O_3 nanocomposites. It is seen that by increasing the Sb_2O_3 content in nanocomposite samples, the m* values get further away from the SPB model, a phenomenon that can be attributed to enhanced energy filtering effect and scattering phenomena at the interfaces. Similar trend has recently been reported in n-type BiTeSe/SnS_2,[26] p-type BiSbTe/Y_2O_3,[17] p-type β-PbZnSb/Cu_3SbSe_4,[35] and p-type BiSbTe/SiO_2 nanocomposites[36] where the authors concluded that getting further from the Pisarenko line is attributed to enhanced energy filtering effect and scattering phenomena at the interfaces.

Moreover, increasing the Sb_2O_3 nanoparticles content from 0 to 4 wt.% resulted in a decrease in the density of state effective mass. However, the rate of decrease in m* was slower than that of p_H in Equation (7), which eventually resulted in an improvement of the Seebeck coefficient. The change in effective mass of the nanocomposites indicates a resonant distortion of the electronic density of states (eDOS) around the Fermi level, since the eDOS is directly related to m*.[35] Without resonant distortion of the eDOS, the Seebeck coefficient would lie in the same line, irrespective of the Sb_2O_3 content. Thus, such resonant distortion effects, by increasing the Sb_2O_3 content, could imply stronger energy filtering in the nanocomposites. (Further evidence on energy filtering effect in the present nanocomposites is provided in Supplementary Information.)

It is known that the optimum electronic performance of a thermoelectric semiconductor depends on the weighted mobility, $\mu(m^*/m_0)^{3/2}$, which includes both the charge carrier mobility (μ) and density-of-states effective mass.[37] Figure 4(c) shows a comparison of the Seebeck coefficient vs. hole mobility and weighted mobility in pure BST and nanocomposite samples at room temperature. It is seen that nanocomposites with higher Sb_2O_3 content (up to 4 wt.%) had larger carrier mobility, due to the reduction of carrier concentration as well as interfacial filtering of low-energy carriers. In addition, the right panel in Figure 4(c) suggests that the maximum thermoelectric power factor (PF) should be observed in BST/4 wt.% Sb_2O_3 samples followed by 6, 2, and 1 wt.% samples. Figure 4(d) depicts a schematic illustration of low-energy hole filtering effect at the interfaces of the BST matrix and Sb_2O_3 nanoparticles. Such energy barriers at the interfaces of hybrid materials can immensely influence the carrier transport characteristics. The present results show that addition of Sb_2O_3 nanoparticles up to 4 wt.% to the BST matrix was effective for energy filtering. But, as observed in Figures 2(d) and (f), there were large nanoparticle agglomerations at the grain boundaries of the 6 wt.% sample. Such non-homogenous distribution of the 2nd phase in the matrix grain boundaries reduced their effective contribution to energy filtering mechanisms.

Figure 4(e) shows the temperature dependence of electrical conductivity in pure BST and BST/Sb_2O_3 nanocomposites. The electrical conductivity declined in all samples with temperature, which corresponds to the degenerate semiconductor behaviour (metal-like nature) of the samples. It is also evident that increasing the Sb_2O_3 content in the nanocomposites reduced the electrical conductivity. The magnified inset of Figure 4(e) shows a clearer trend in electrical conductivity decline by increasing the nanoparticle concentration at room temperature. There was a maximum reduction of 10.1 % in electrical conductivity of the pure BST after adding 6 wt.% Sb_2O_3 at room temperature, and this difference became larger at higher temperatures and reached 18.5 % at 475 K. Electrical conductivity of a p-type semiconductor depends on its carrier concentration and mobility, described as $\sigma = \mu.p.e$, in which e is the charge of the carriers. By adding Sb_2O_3 nanoparticles up to 4 wt.% to the BST matrix, the carrier concentration decreased, but the carrier mobility increased (at a slower rate). As a result, the electrical conductivity decreased mainly due to the reduction of carrier concentration which occurred due to a band-structure mismatch between the matrix material and the nanoparticles.[38, 39]

To determine the electronic transport efficiency of a thermoelectric material the power factor is used, which is calculated by the Seebeck coefficient and electrical conductivity as $PF = \sigma S^2$. The temperature dependence of the power factor of the BST alloy and its nanocomposites are shown in Figure 4(f). It is noticed that the PF of all the samples decrease with temperature. In general, adding Sb_2O_3 nanoparticles up to 4 wt.% increased the PF, but the 6 wt.% sample had smaller PF than the 4 wt.% sample at all tested temperatures. The PF of the 1 wt.% sample was slightly lower than that of the pure BST up to 325 K due to the large decline of the electrical conductivity after adding Sb_2O_3 nanoparticles to the matrix. But at higher temperatures, the PF of the 1 wt.% sample was compensated by the higher Seebeck coefficient. There was a 14% improvement in the PF of the 4 wt.% sample

This journal is © The Royal Society of Chemistry 20xx

Please do not adjust margins

at room temperature as compared to the BST alloy, and this enhancement was as large as 34% at 425 K.

Figure 5 represents the thermal transport properties of pure BST and BST/Sb_2O_3 nanocomposites as a function of temperature. As shown in Figure 5a, the total thermal conductivity (K_{tot}) of all samples gradually decreased with temperature, and after reaching a minimum point it increased. Adding Sb_2O_3 nanoparticles decreased K_{tot} in the whole tested temperature range, and by increasing the Sb_2O_3 content, K_{tot} decreased further. In the 6 wt.% Sb_2O_3 sample, there was a 5.2% decline of K_{tot} at room temperature as compared to pure BST. This trend was escalated at higher temperatures and reached 14.5% at 475 K. The lowest value of K_{tot} for the pure BST was observed at 325 K, however by addition of Sb_2O_3 nanoparticles, minimum K_{tot} gradually shifted to 325 K and 350 K. This means that he bipolar effects were moved to higher temperatures in the nanocomposite samples.

To further analyse the thermal properties of the samples, the total thermal conductivity was separated into two components, electronic thermal conduction (K_e) and lattice (phonon) thermal conduction (K_{lat}). The electronic component of thermal conductivity was calculated from the Wiedmann-Franz's law, describes as $K_e = L.\sigma.T$, in which, L is the Lorenz number, calculated using the Fermi integral function (Figure 5(b)).[40] Figure 5(c) shows that the electronic component of thermal conductivity decreases significantly by adding Sb_2O_3 nanoparticles, which could be due to the intensified carrier scattering/filtering by the newly generated BST/Sb_2O_3 interfaces/potential barriers in the microstructure. [17, 19, 20, 41] Moreover, in general K_e decreased with temperature in all samples. The observed exception was related to pure BST and 1 wt.% nanocomposite whose K_e slightly increased after 425 K.

The phononic component of thermal conductivity however showed a different trend, that is K_{lat} marginally increased up to 375 K and then escalated rapidly at higher temperatures (Figure 5 (d)). At room temperature, the nanocomposite samples had a larger K_{lat} than pure BST, suggesting that Sb_2O_3 nanoparticles did not have a positive impact on phonon scattering. However at higher temperatures, K_{lat} of the nanocomposites was smaller than that of pure BST. Earlier research shows that reduction of K_{lat} in nanocomposites strongly depends on the size of nanoparticles, and vigorous phonon scattering could be observed when the particle size is smaller than 10 nm.[42] As the size of the dispersed Sb_2O_3 nanoparticles in this work was in the order of 10s of nanometres, the electrons were more strongly scattered than phonons; hence, the electronic component of thermal conductivity had a bigger contribution in reduction of total thermal conductivity in BST/Sb_2O_3 nanocomposites.

The thermoelectric figure of merit (ZT) is a measure of the competition between electronic transport (i.e. power factor) and thermal transport (i.e. total thermal conductivity). The temperature dependence of ZT for pure BST and its nanocomposites is shown in Figure 6(a). In general, nanocmposite samples had a higher ZT than pure BST due to their simultaneous power factor enhancement and thermal conductivity reduction. The only exception was related to 1 wt.% samples that had a slightly lower ZT than pure BST up to 325 K. Further addition of Sb_2O_3 nanoparticles up to 4 wt.% improved the ZT of the nanocomposites at all temperatures, but the 6 wt.% samples had a marginally lower ZT than the 4 wt.% samples. The maximum ZT of pure BST was 1.2 obtained at 325 K. However, by addition of Sb_2O_3 nanoparticles the maximum ZT of the nanocomposites was shifted to 350 K. The 4 wt.% samples had the highest ZTs among all, and demonstrated an encouraging ZT of ~1.5 at 325 K and 350 K. Nanocomposite samples with 2, 4, and 6 wt.% Sb_2O_3 maintained their large ZT levels even at higher temperatures, and had ZT>1 from room temperature up to 450 K. That is, the BST/Sb_2O_3 nanocomposite samples can exhibit excellent thermoelectric efficiency for a much larger temperature range than pure BST alloys.

To further evaluate the stability and suitability of BST/Sb_2O_3 nanocomposites for thermoelectric applications, time-dependent property measurements were performed during a 2-year time span. For these measurements, 4 samples of BST/4 wt.% Sb_2O_3 were initially sintered and kept at ambient condition (i.e., temperature range: 293 K-298 K, and humidity range: ~50-60~). Every 6 months, one sample was tested 3 times to calculate the average ZT values, as shown in Figure 6(b). The ZT values at room temperature and 350 K (max ZT values) decreased only by 4.2 % and 6.6 %, respectively, after 2 years of exposure to ambient atmosphere. These results demonstrate that the prepared nanocomposites are very stable at open-air benchtop condition, and considering their ZT enhancement via energy filtering effect, we envisage great potential for their thermoelectric applications at a wide temperature range (300– 450 K).

4. Conclusions

In summary, p-type BST/X wt.% Sb_2O_3 (X= 0, 1, 2, 4, 6) nanocomposite disks were fabricated from a mixture of micro- and nano-sized BST powders blended with Sb_2O_3 nanoparticles, and consolidated by spark plasma sintering. The simultaneous optimisation of electrical and thermal properties was achieved by controlling the Sb_2O_3 content in the microstructure of the nanocomposites. Electrical conductivity decreased (max 18 %) after adding Sb_2O_3 nanoparticles to the microstructure due to decline in charge carrier concentration. But, the enhancement of Seebeck coefficient (up to 24 %) and power factor (up to 34 %) due to low-energy hole filtering effect compensated for that, and improved the ZT values up to 39% at room temperature and 53% at 450 K. A peak ZT of 1.51 was obtained at 350 K by addition of 4 wt.% Sb_2O_3 nanoparticles to the BST alloy. A unique feature of this research was the time-dependent ZT measurements on BST/Sb_2O_3 nanocomposites, which demonstrated the stability of the products at ambient condition over a 24-month course. A maximum of 6.6 % reduction in the ZT value was observed in

that period, suggesting the excellent chemical and thermal stability of the nanocomposites.

Conflicts of interest

There are no conflicts to declare.

Acknowledgements

AP acknowledges the financial support of the Japan Society for the Promotion of Science (JSPS) ID No. 14332. TM acknowledges CREST JPMJCR15Q6 and JSPS KAKENHI JP17H02749 funding. VN acknowledges European Research Council Consolidator Grant (ERC-CoG) Project ID: 681544. AP is grateful to NIMS Transmission Electron Microscopy Station for their technical support.

Notes and references

1. L. E. Bell, *Science*, 2008, **321**, 1457-1461.
2. T. Mori and S. Priya, *MRS Bull.*, 2018, **43**, 176-180.
3. M. S. Dresselhaus, G. Chen, M. Y. Tang, R. G. Yang, H. Lee, D. Z. Wang, Z. F. Ren, J. P. Fleurial and P. Gogna, *Adv. Mater.*, 2007, **19**, 1043-1053.
4. G. J. Snyder and E. S. Toberer, *Nat. Mater.*, 2008, **7**, 105-114.
5. T. Mori, *Small*, 2017, **13**, 1702013.
6. W. Kim, J. Zide, A. Gossard, D. Klenov, S. Stemmer, A. Shakouri and A. Majumdar, *Phys. Rev. Lett.*, 2006, **96**, 045901.
7. J. H. Bahk and A. Shakouri, *Appl. Phys. Lett.,* 2014, **105**, 052106.
8. L. D. Zhao, S. H. Lo, J. Q. He, H. Li, K. Biswas, J. Androulakis, C. I. Wu, T. P. Hogan, D. Y. Chung, V. P. Dravid and M. G. Kanatzidis, *J. Am. Chem. Soc.*, 2011, **133**, 20476-20487.
9. J. M. O. Zide, D. Vashaee, Z. X. Bian, G. Zeng, J. E. Bowers, A. Shakouri and A. C. Gossard, *Phys. Rev. B*, 2006, **74**, 205335.
10. A. Shakouri, *Annu. Rev. Mater. Res.*, 2011, **41**, 399-431.
11. M. Zebarjadi, G. Joshi, G. H. Zhu, B. Yu, A. Minnich, Y. C. Lan, X. W. Wang, M. Dresselhaus, Z. F. Ren and G. Chen, *Nano Lett.*, 2011, **11**, 2225-2230.
12. D. Narducci, E. Selezneva, G. Cerofolini, S. Frabboni and G. Ottaviani, *J. Solid State Chem.*, 2012, **193**, 19-25.
13. K. Nishio and T. Hirano, *Jpn. J. Appl. Phys. 1*, 1997, **36**, 170-174.
14. B. Poudel, Q. Hao, Y. Ma, Y. C. Lan, A. Minnich, B. Yu, X. A. Yan, D. Z. Wang, A. Muto, D. Vashaee, X. Y. Chen, J. M. Liu, M. S. Dresselhaus, G. Chen and Z. F. Ren, *Science*, 2008, **320**, 634-638.
15. W. Xie, J. He, H. J. Kang, X. Tang, S. Zhu, M. Laver, S. Wang, J. R. Copley, C. M. Brown, Q. Zhang and T. M. Tritt, *Nano Lett.*, 2010, **10**, 3283-3289.
16. Y. C. Q. Dou, X. Y., D. Li, L. L. Li, T. H. Zou and Q. Q. Wang, *J. Appl.Phys.*, 2013, **114**, 044906.
17. B. Madavali, H.-S. Kim, K.-H. Lee and S.-J. Hong, *Intermetallics*, 2017, **82**, 68-75.
18. Y. Li, Y. Dou, X. Qin, J. Zhang, H. Xin, D. Li, C. Song, T. Zou, Y. Liu and C. Li, *RSC Advances*, 2016, **6**, 12243-12248.
19. F. Li, X. Huang, Z. Sun, J. Ding, J. Jiang, W. Jiang and L. Chen, *J. Alloy. Comp.*, 2011, **509**, 4769-4773.
20. J. Li, Q. Tan, J.-F. Li, D.-W. Liu, F. Li, Z.-Y. Li, M. Zou and K. Wang, *Adv. Funct. Mater.*, 2013, **23**, 4317-4323.
21. D. Li, J. M. Li, J. C. Li, Y. S. Wang, J. Zhang, X. Y. Qin, Y. Cao, Y. S. Li and G. D. Tang, *J. Mater. Chem. A*, 2018, **6**, 9642-9649.
22. B. Madavali, C. H. Lee, H. S. Kim, K. H. Lee and S. J. Hong, *Int. J. Appl. Ceram. Tec.*, 2018, **15**, 125-131.
23. Y. Pan, U. Aydemir, F.-H. Sun, C.-F. Wu, T. C. Chasapis, G. J. Snyder and J.-F. Li, *Adv. Science*, 2017, **4**, 1700259.
24. D. W. Liu, J. F. Li, C. Chen and B. P. Zhang, *J. Electron. Mater.*, 2011, **40**, 992-998.
25. Z. Song, Q. Zhang, Y. Liu, Z. Zhou, X. Lu, L. Wang, W. Jiang and L. Chen, *Phys. Status Solidi A*, 2017, **214**, 1600451.
26. S. K. Li, X. R. Liu, Y. D. Liu, F. S. Liu, J. Luo and F. Pan, *Nano Energy*, 2017, **39**, 297-305.
27. X. Y. Wang, Y. Yu, B. Zhu, N. Gao, Z. Y. Huang, B. Xiang and F. Q. Zu, *J. Electron. Mater.*, 2018, **47**, 998-1002.
28. B. L. Cao, J. K. Jian, B. H. Ge, S. M. Li, H. Wang, J. Liu and H. Z. Zhao, *Chinese Phys. B*, 2017, **26**.
29. S. J. Jung, S. Y. Park, B. K. Kim, B. Kwon, S. K. Kim, H. H. Park, D. I. Kim, J. Y. Kim, D. B. Hyun, J. S. Kim and S. H. Baek, *Acta Mater.*, 2015, **97**, 68-74.
30. G. S. Nolas, Yang, J., Goldsmid, H.J., in *Thermal Conductivity: Theory, Properties, and Applications*, ed. T. M. Tritt, Kluwer Academic / Plenum Publishers, 2010, DOI: 10.1007/b136496, pp. 123-152.
31. J. W. Shen, Z. W. Chen, S. Q. Lin, L. L. Zheng, W. Li and Y. Z. Pei, *J. Mater. Chem. C*, 2016, **4**, 209-214.
32. P. H. M. Bottger, G. S. Pomrehn, G. J. Snyder and T. G. Finstad, *Phys. Status Solidi A*, 2011, **208**, 2753-2759.
33. C. L. Chen, H. Wang, Y. Y. Chen, T. Day and G. J. Snyder, *J. Mater. Chem. A*, 2014, **2**, 11171-11176.
34. J. P. Wiff, Y. Kinemuchi, H. Kaga, C. Ito and K. Watari, *J. Eur. Ceram. Soc.*, 2009, **29**, 1413-1418.
35. T. Zou, X. Qin, Y. Zhang, X. Li, Z. Zeng, D. Li, J. Zhang, H. Xin, W. Xie and A. Weidenkaff, *Sci. Rep.*, 2015, **5**, 17803.
36. Y. C. Dou, X. Y. Qin, D. Li, L. L. Li, T. H. Zou and Q. Q. Wang, *J. Appl. Phys.*, 2013, **114**, 044906.
37. Y. Z. Pei, A. D. LaLonde, H. Wang and G. J. Snyder, *Energ. Environment. Sci.*, 2012, **5**, 7963-7969.
38. Y. Y. Li, D. Li, X. Y. Qin, X. H. Yang, Y. F. Liu, J. Zhang, Y. C. Dou, C. J. Song and H. X. Xin, *J. Mater. Chem. C*, 2015, **3**, 7045-7052.
39. Y. Y. Li, X. Y. Qin, D. Li, J. Zhang, C. Li, Y. F. Liu, C. J. Song, H. X. Xin and H. F. Guo, *Appl. Phys. Lett.*, 2016, **108**.
40. H. S. Kim, Z. M. Gibbs, Y. L. Tang, H. Wang and G. J. Snyder, *Apl. Mater.*, 2015, **3**.
41. E. B. Kim, P. Dharmaiah, D. Shin, K. H. Lee and S. J. Hong, *J. Alloy. Comp.*, 2017, **703**, 614-623.
42. J. S. Son, K. Park, M. K. Han, C. Kang, S. G. Park, J. H. Kim, W. Kim, S. J. Kim and T. Hyeon, *Angew. Chem. Int. Edit.*, 2011, **50**, 1363-1366.

This journal is © The Royal Society of Chemistry 20xx

Please do not adjust margins

Figure Captions

Figure 1. (a) SEM image and EDS analysis of micro- and nano-sized powders of BST mixed with Sb_2O_3 nanoparticles. (b, c) XRD patterns of pure BST and a nanocomposite sample with 6 wt.% Sb_2O_3 after SPS. (d) EDS line scan analysis of a sintered nanocomposite sample.

Figure 2. (a-d) Fracture surface SEM images of pure BST and its nanocomposites with 1, 4, and 6 wt.% Sb_2O_3. (e, f) Higher magnification images of (b) and (d), respectively. Accumulation of Sb_2O_3 nanoparticles at the grain boundaries is evident, especially in (f).

Figure 3. (a, b) High resolution TEM images of sintered BST. (c) Selected area electron diffraction pattern of sintered BST. (d) Atomic structure representation of BST. (e) Dark-field STEM image of a nanocomposite sample and its corresponding EDS line-scan analysis.

Figure 4. (a) Temperature dependence of Seebeck coefficient in BST/X wt.% Sb_2O_3 (X=0, 1, 2, 4, 6). (b) Seebeck coefficient vs. carrier concentration at 300 K. (c) Seebeck coefficient vs. carrier mobility and weighted mobility. (d) A schematic representation of low-energy hole filtering effect in BST/Sb_2O_3 nanocomposites. (e, f) Temperature dependence of electrical conductivity and power factor.

Figure 5. Temperature dependence of (a) total thermal conductivity, (b) Lorentz number, (c) electronic component of thermal conductivity, and (d) lattice component of thermal conductivity in BST/X wt.% Sb_2O_3 (X=0, 1, 2, 4, 6).

Figure 6. Temperature dependence of figure of merit for (a) BST/X wt.% Sb_2O_3 (X=0, 1, 2, 4, 6), and (b) BST/4 wt.% Sb_2O_3 during a 24-months span.

This journal is © The Royal Society of Chemistry 20xx

Please do not adjust margins

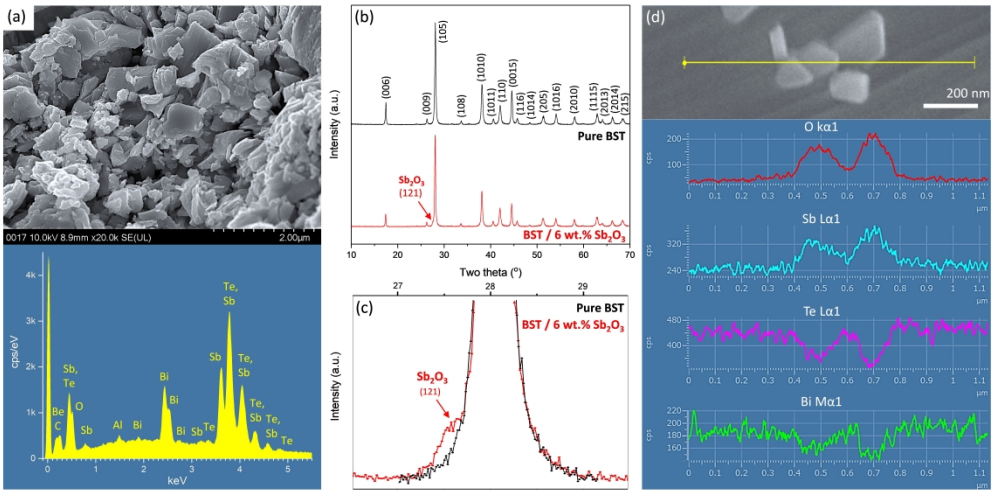

Figure 1. (a) SEM image and EDS analysis of micro- and nano-sized powders of BST mixed with Sb2O3 nanoparticles. (b, c) XRD patterns of pure BST and a nanocomposite sample with 6 wt.% Sb2O3 after SPS. (d) EDS line scan analysis of a sintered nanocomposite sample.

1619x800mm (120 x 120 DPI)

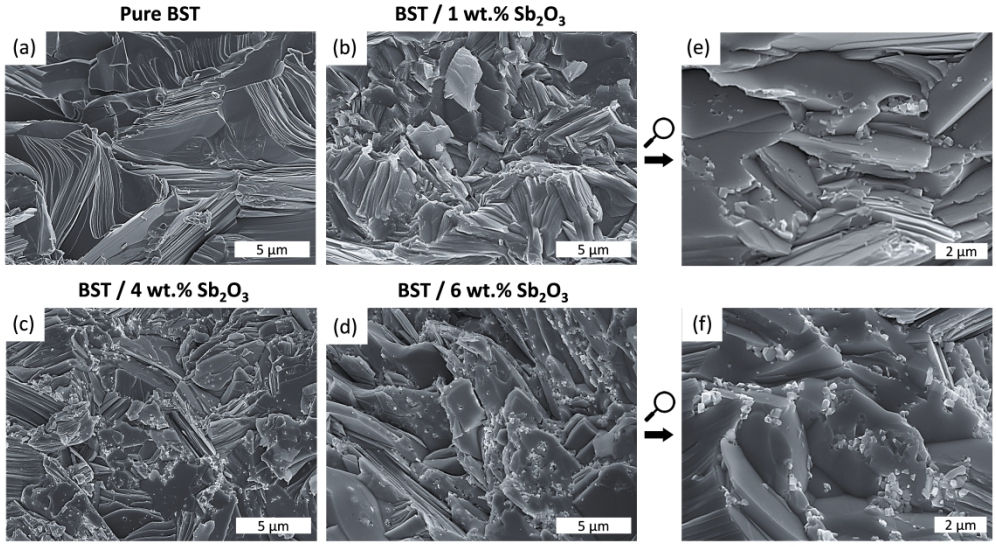

Figure 2. (a-d) Fracture surface SEM images of pure BST and its nanocomposites with 1, 4, and 6 wt.% Sb2O3. (e, f) Higher magnification images of (b) and (d), respectively. Accumulation of Sb2O3 nanoparticles at the grain boundaries is evident, especially in (f).

1287x716mm (120 x 120 DPI)

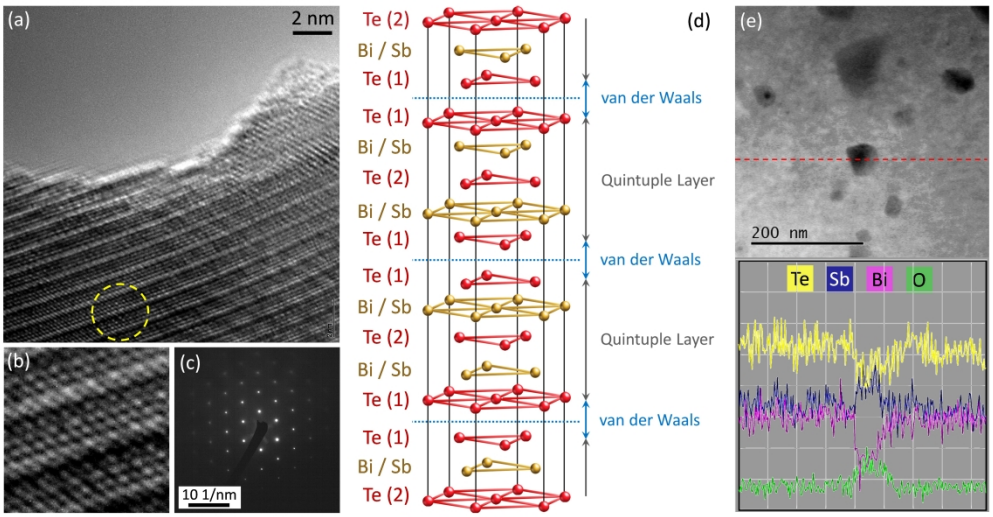

Figure 3. (a, b) High resolution TEM images of sintered BST. (c) Selected area electron diffraction pattern of sintered BST. (d) Atomic structure representation of BST. (e) Dark-field STEM image of a nanocomposite sample and its corresponding EDS line-scan analysis.

1337x693mm (120 x 120 DPI)

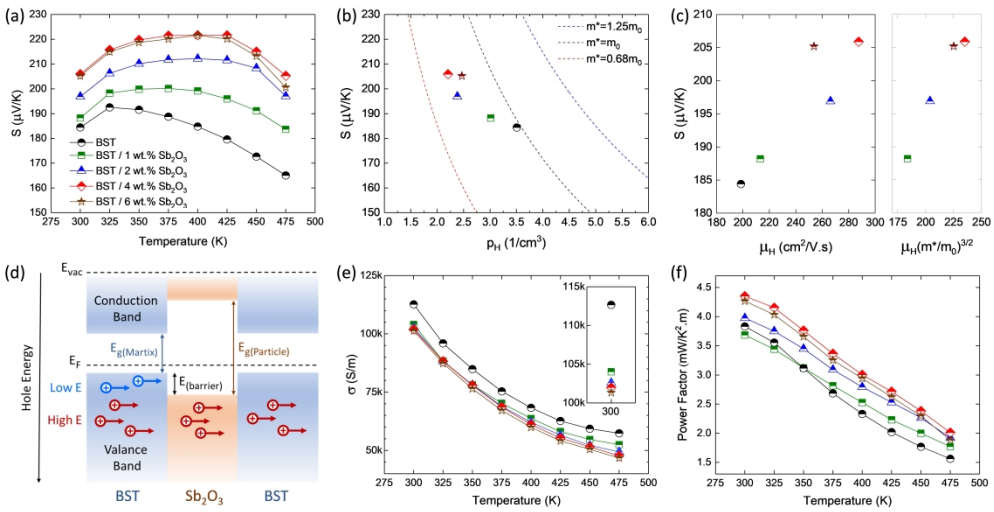

Figure 4. (a) Temperature dependence of Seebeck coefficient in BST/X wt.% Sb2O3 (X=0, 1, 2, 4, 6). (b) Seebeck coefficient vs. carrier concentration at 300 K. (c) Seebeck coefficient vs. carrier mobility and weighted mobility. (d) A schematic representation of low-energy hole filtering effect in BST/Sb2O3 nanocomposites. (e, f) Temperature dependence of electrical conductivity and power factor.

1512x780mm (120 x 120 DPI)

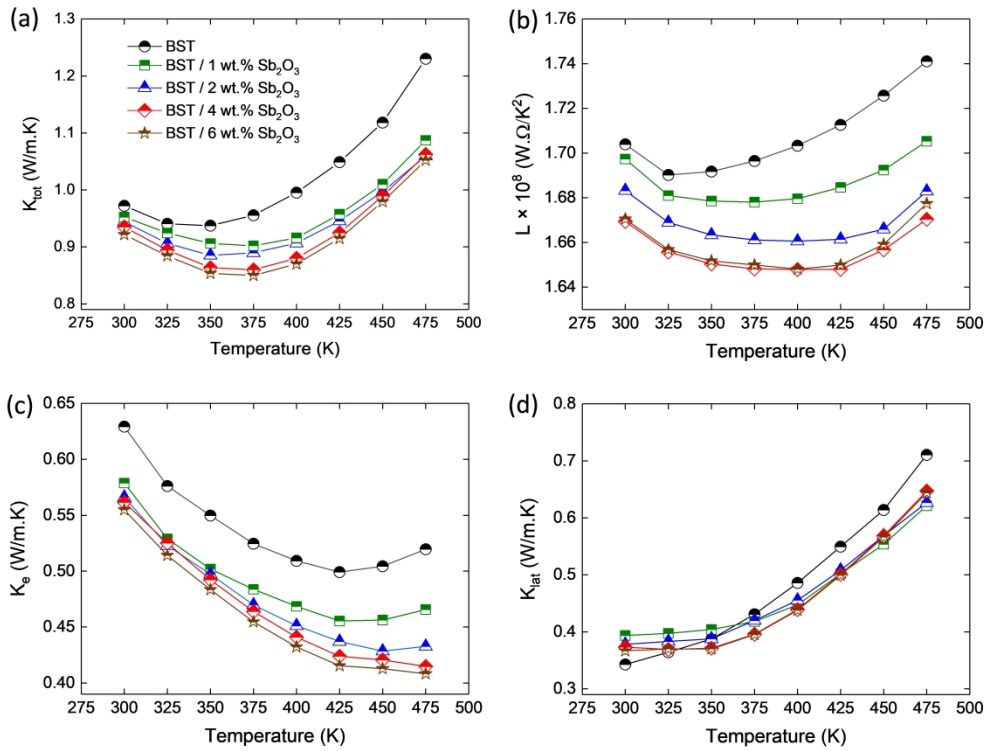

Figure 5. Temperature dependence of (a) total thermal conductivity, (b) Lorentz number, (c) electronic component of thermal conductivity, and (d) lattice component of thermal conductivity in BST/X wt.% Sb2O3 (X=0, 1, 2, 4, 6).

1030x779mm (120 x 120 DPI)

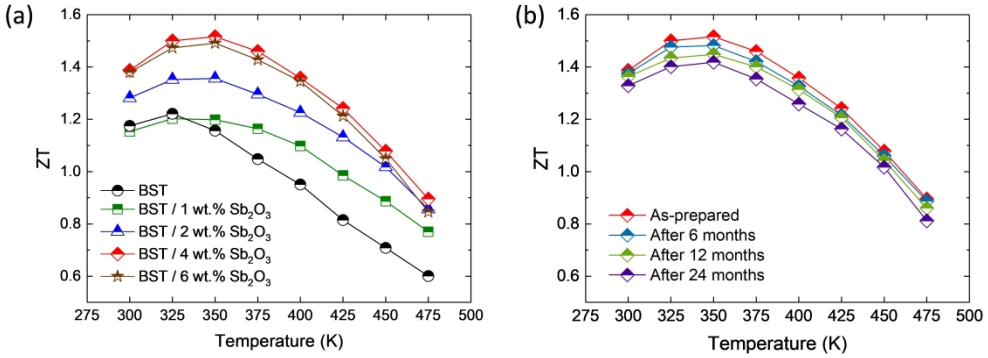

Figure 6. (a) Temperature dependence of figure of merit for BST/X wt.% Sb2O3 (X=0, 1, 2, 4, 6). (b) for BST/4 wt.% Sb2O3 during a 24-months span.

1040x386mm (120 x 120 DPI)

24-month high-ZT stability of $Bi_{0.5}Sb_{1.5}Te_3/Sb_2O_3$ nanocomposites that demonstrate simultaneous Seebeck coefficient enhancement and thermal conductivity decline through energy filtering effect.

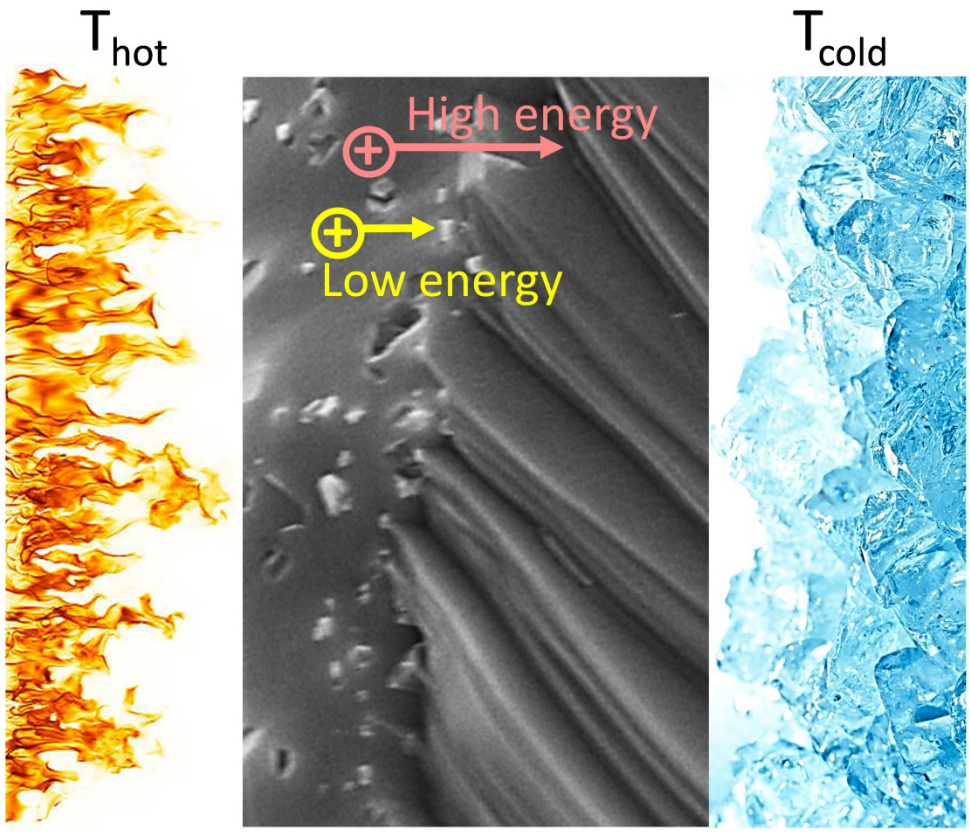

677x619mm (120 x 120 DPI)